Applied Physics A (2022) 128:1028
https://doi.org/10.1007/s00339-022-06180-x

Applied Physics A
Materials Science & Processing

Physical, structural, optical, and gamma ray shielding properties of Li_2O–ZnO–SiO_2–P_2O_5 glasses doped with Nd_2O_3

Mohammed A. Algradee[1,2] · Emran Eisa Saleh[3] · O. M. Samir[1,4] · Abduelwhab B. Alwany[1] · Tharwat M. El-Sherbini[2]

Received: 17 July 2022 / Accepted: 25 October 2022 / Published online: 4 November 2022

Abstract

Novel Li_2O–ZnO–SiO_2–P_2O_5 glasses doped with Nd_2O_3 have been prepared via the ordinary melt-quenching technique. Density and molar volume, FTIR spectra, and UV–visible absorption spectroscopy were used to investigate the physical, structural, and optical properties of glasses. The density increases from 2.545 to 2.644 $g.cm^{-3}$ and the molar volume decreases from 38.158 to 37.794 cm^3 mol^{-1}. The values of the optical gap energies of the samples increased from 3.331 to 3.712 eV with the addition of Nd^{3+} ions. The results of the infrared spectra analysis showed many vibration modes, and it was found that the intensity of both P–O^- and Si–O^- vibration modes decreases with the increase in Nd^{3+} ions, which confirms the increase in the bridging oxygen (BO). The theoretical optical basicity ($\Lambda_{th.}$) values increased from 1.205 to 1.238, while the interaction (A) values decreased from 0.2209 to 0.2189 $Å^3$. The nuclear radiation shielding parameters, such as mass attenuation coefficient, mean free path, half-value layer, effective atomic number, and electron density, were estimated using Phy-X/PSD and XCOM software programs. The effect of Nd_2O_3 content on radiation protection properties was evaluated. The results showed that the LiZnSiP:4Nd glass sample gave the best protection against gamma and neutron radiation.

Keywords Silicophosphate glasses · Physical and optical properties · FTIR analysis · Gamma-ray shielding

1 Introduction

Phosphate glasses have attracted a lot of attention over the last few decades due to their unique features that make them appropriate for a wide range of applications. They have been used in a wide range of applications, including medicine, biology, optics, and electronics, due to their reduced melting and softening temperatures, strong electric conductivity, and optical properties [1–6]. Furthermore, due to their high ionic conductivity, low melting point, and strong glass-forming property, alkali phosphate glasses have gained popularity [7, 8]. However, it is generally known that phosphate glasses are chemically unstable, volatile, and hygroscopic. These properties reduce the stability of these glasses and limit their usage in a variety of technological applications. The insertion of certain alkali oxides, such as Li_2O, in phosphate glass compositions improves the mechanical properties of the glass network. Li_2O serves as a vacancy generator, enhances the network connectivity, and increases the capacity to generate non-bridging oxygen (NBO) [9]. ZnO can enter the glass matrix as ZnO_4 or P–O–Zn bridge [10]. The formation of these bonds leads to increase in the chemical durability of phosphate glasses [11]. ZnO can also acts as network modifier and its cation (Zn^{2+})

✉ Mohammed A. Algradee
algradi772001@yahoo.com

Emran Eisa Saleh
eesas2009@yahoo.com

O. M. Samir
samirbas@gmail.com

Abduelwhab B. Alwany
abdualwhab@yahoo.com

Tharwat M. El-Sherbini
Thelsherbini@hotmail.com

[1] Physics Department, Science Faculty, Ibb University, 70270 Ibb, Yemen

[2] Laboratory of Lasers and New Materials, Faculty of Science, Cairo University, Giza 12613, Egypt

[3] Physics Department, Faculty of Science, University of Aden, Aden, Yemen

[4] Aljanad University for Science and Technology, Taiz, Yemen

occupies interstitial sites in network of glasses [12, 13]. The pure silicon dioxide glass type, commonly known as fused silica, does not absorb UV radiation. It is extensively cross-linked in three dimensions, resulting in a low coefficient of expansion and suitability for usage at high temperature conditions [14]. Phosphate-containing silicon is a common and important chemical system in bioactive glass and metallurgical slag. Silicon can have a major impact on the phase relationships and physicochemical characteristics of silicon-containing bioglasses or steelmaking slags. Both phosphorus and silicon are capable of constructing networks in silicon-containing phosphate systems and may generate "mixed network formation effect", which characterizes the unexpected variations in physical characteristics as a function of composition in the glass having more than one framework component. Given the structural behaviour of silicon in phosphate, this is especially important for bioglass manufacturing or steelmaking [15]. Because the gamma photon lacks mass and charge, it is regarded as one of the most ionizing and dangerous radiations. As these rays are transmitted over long distances and have a high ability to penetrate materials and pass through human bodies, exposure to these rays for a long time leads to serious damage such as the destruction of blood cells, skin diseases, and the destruction of DNA molecules, in addition to genetic diseases that may lead to death. For these reasons, many research groups have focused their attention on the production of various shielding materials that protect against these rays, to be used as an alternative to those commonly used in this field, such as concrete, rocks, alloys, and polymers, which are good materials for shielding against these rays, but they are opaque. Therefore, the efforts of researchers were directed to focus on studying glass materials as an alternative to the common materials in this aspect, because they are more suitable for their high transparency, ease of preparation and formation, and the availability of raw materials used in preparation [16–19]. Trivalent Nd^{3+} ions have been widely studied among the rare earth (R.E.) ions [18–21] due to their high laser effectiveness and 1.3 m luminescence, which may be exploited for optical amplification in the near infrared (NIR) range [22]. Although there are many spectroscopic studies of glass doped with neodymium ions, there is a lack of studies on the structural characteristics and the physical, optical, and shielding properties against gamma rays, especially in this new type of glass that has been prepared. As a result, the purpose of this work is to create novel Li_2O–ZnO–SiO_2–P_2O_5 glasses doped with Nd_2O_3 and estimate the impact of these additions on the structural, physical, and gamma-ray shielding. In addition, the molar refraction, refractive index, molar polarizability, and metallization criteria of the materials were calculated based on the optical band gap that was determined by Tauc's method. The results of the study gave comprehensive knowledge about the possibility of using prepared glass as gamma ray shields. It is known that the materials used as gamma ray shields must have higher mass attenuation coefficient (MAC) values, as well as lower half-value layer (HVL), and mean free path (MFP). Through our current study, it was found that the prepared glass gave values for the mass attenuation coefficient higher than the values of the mass attenuation coefficient for ordinary concrete used as gamma ray shielding, as well as superiority to the glass named Rs 520 G18 at the lower energy values of gamma rays.

2 Experimental methods

LiZnSiP:ND glasses with the composition of [20 mol% Li_2O–10 mol% ZnO–20 mol% SiO_2–50 mol% P_2O_5:x wt% Nd_2O_3] with $x = 0.0$(LiZnSiP:0Nd) to 4.0 (LiZnSiP:4Nd) were prepared via ordinary melt-quenching technique. Anhydrous powders of high purity Li_2CO_3, ZnO, P_2O_5, SiO_2, and Nd_2O_3 were chosen. Appropriate quantities of chemicals were ground and stirred in an agate mortar, and the batches were preheated in porcelain crucible at 300 °C for 1.0 h. This procedure allows the P_2O_5 to dissolve and react with Li_2CO_3, SiO_2, ZnO, and Nd_2O_3 before melting. The mixture was melted at a temperature of 1300 °C for 1 h, during which the samples were stirred several times to ensure the homogeneity process. After that, the molten was poured onto stainless steel plates heated at a temperature of 300 °C, and the samples were immediately entered into a furnace at a temperature of 350 °C for 1 h to remove the mechanical stress within the glasses. Following that, the furnace was turned off and left to cool until the temperature reached room temperature. The synthesized samples are

Table 1 Code and chemical composition of the studied glasses

Sample code	Composition (mol%)					Composition (mol%)				
	Li_2O	ZnO	SiO_2	P_2O_5	Nd_2O_3 (wt%)	Li_2O	ZnO	SiO_2	P_2O_5	Nd_2O_3
LiZnSiP:0Nd	20	10	20	50	0	20	10	20	50	0
LiZnSiP:0.25Nd	20	10	20	50	0.25	19.98515	9.992576	19.98515	49.96288	0.074243
LiZnSiP:0.5Nd	20	10	20	50	0.5	19.97032	9.985162	19.97032	49.92581	0.148377
LiZnSiP:1Nd	20	10	20	50	1	19.94074	9.970369	19.94074	49.85184	0.296314
LiZnSiP:2Nd	20	10	20	50	2	19.88182	9.940912	19.88182	49.70456	0.590877
LiZnSiP:4Nd	20	10	20	50	4	19.76504	9.882519	19.76504	49.41259	1.174812

marked by LiZnSiP:0Nd, LiZnSiP:0.25Nd, LiZnSiP:0.5Nd, LiZnSiP:1Nd, LiZnSiP:2Nd, and LiZnSiP:4Nd (Table 1).

The glass density (ρ) was determined using Archimedes' method and Eq. (1):

$$\rho = [\rho_{\text{toluene}} \frac{\left(M_{\text{g.a.}} - M_{\text{l.a.}}\right)}{\left(M_{\text{g.a.}} - M_{\text{l.a.}}\right) - \left(M_{\text{g.t.}} - M_{\text{l.t.}}\right)}] \quad (1)$$

where ρ_{toluene} is the toluene density ($\rho_{\text{toluene}} = 0.866$ g cm^{-3}), the parameters ($M_{\text{g.a}}$, $M_{\text{l.a.}}$, $M_{\text{g.t.}}$, and $M_{\text{l.t.}}$) are the mass of the glass in air, the mass of suspended thread in air, the mass of the glass in toluene, and the mass of suspended thread in toluene, respectively. To evaluate the uncertainty in the ρ and molar volume (V_m), each sample was repeated three times ($N = 3$). The following expression is used to calculate the density's uncertainty [23]:

$$\rho = \frac{\sum \rho}{N} \pm \Delta\rho_{\text{avg.}} \quad (2)$$

where $\Delta\rho_{\text{avg.}} = \frac{\rho_{\max} - \rho_{\min}}{2\sqrt{N}}$.

and the molar volume was computed by Eq. (3):

$$\text{V}_{\text{m}} = \frac{M_{\text{w}}}{\rho} \quad (3)$$

The error in the molar volume is [23]:

$$\text{V}_{\text{m}} = \frac{\sum V_{\text{m}}}{N} \pm \frac{M_{\text{w}} \times \Delta\rho_{\text{avg.}}}{\rho^2} \quad (4)$$

where M_w is the molecular weight of glass.

The absorption (A) spectra were obtained with a spectrophotometer Jasco V-570 Corp. (190–1000 nm). All of the optical spectra measurement conditions were fixed, and the samples were recorded within the UV–Vis spectrophotometer using an air reference with a spectral resolution of ± 2 nm.

The FTIR spectra of specimens were obtained using the KBr disc method on a JASCO FT/IR-460 plus (Japan) spectrometer with a spectral resolution of ± 0.964233 cm^{-1} in the 4000–400 cm^{-1} range. The potassium bromide (KBr) disc technique was used in conjunction with an infrared spectrometer. Glass samples weighing 0.004 g were ground and mixed with 0.200 g of KBr. After that, the mixture was pressed at 15 tons for 3 min under vacuum to yield transparent discs suitable for mounting in the spectrometer. The intensities of all FTIR spectra were determined using spectra manager software.

The mass attenuation coefficient (MAC), the mean free path (MFP), the half-value layer (HVL), the effective atomic number (Z_{eff}), and electron density (N_{eff}) were evaluated to know the radiation penetration in the prepared samples using Phy-X/PSD and XCOM programs [24, 25]. The MAC is the main factor for knowing the interaction of radiation with matter and depends on the cross-sections of the interaction and the energy of the photon. Using this parameter, other nuclear parameters such as HVL, MFP, Z_{eff} and N_{eff} can be estimated. Phy-X/PSD is a new and important program for knowing the gamma-protective properties of materials. Also, the effective removal cross-sections for fast neutrons are evaluated. The database used to calculate the nuclear parameters such as the mass attenuation coefficient (MAC) and other parameters such as HVL, MFP, Z_{eff}, and N_{eff} by Phy-X/PSD and XCOM are the chemical composition of the sample and the percentages of each element in the compound, as well as the density of the prepared glass sample (ρ). The theoretical basis for the computed shielding parameters are shown in these works [26, 27].

3 Results and discussion

3.1 Physical properties

The density is regarded as a critical tool for detecting structural changes within the glass network caused by variations in glass composition. Modifier ion fluctuations can produce changes in the dimensions of the glass's interstitial space, geometrical configuration, cross-link density, and coordination number. Table 2 lists both the ρ and V_m values of samples and depicts them in Fig. 1. The rise in Nd_2O_3 concentration caused ρ to rise from 2.545 to 2.644 g cm^{-3} and V_m to reduce from 38.158 to 37.794 cm^3 mol^{-1}. The increase in the ρ may be attributed to the fact that the molecular weight of Nd_2O_3 (336.48 g mol^{-1}) is higher than the molecular weight of other oxides in the LiZnSiP:Nd glasses (ZnO = 81.38 g mol^{-1}, SiO_2 = 60.08 g mol^{-1}, P_2O_5 = 141.94 g mol^{-1} and Li_2O = 29.88 g mol^{-1}) ;hence, the current glass system becomes more dense. In addition, the silicophosphate network includes a high number of interstices, and when Nd^{3+} ions are introduced, they fill these vacancies, increasing the density of the glass structure. There are two modifiers in the prepared glasses: lithium and neodymium, which can fill these interstitial gaps. The decrease in V_m can be attributed to increase in structural compactness caused by the creation of P–O–Zn and P–O–Nd ionic bonds. Also, the increased ρ is owing to the larger atomic mass of neodymium ions in the glass system in comparison to other oxides in the glass matrix; hence, the increased oxygen packing density (OPD) makes the system more compact. The behaviour of V_m is diametrically opposed to that of ρ.

The concentrations of Nd^{3+} ions (N_{Nd}), polaron radius (r_p), field strength (F), and interatomic distance (r_i) are determined using the following equations [28] and recorded in Table 2.

$$N_{\text{Nd}} = \rho N_{\text{A}} (\text{mol\% of Nd}) / M_{\text{w}} \quad (5)$$

Table 2 Density (ρ), molar volume (V_m), the molecular weight of glass (M_w), Nd^{3+} ion concentration (N_{Nd}), polaron radius (r_p), inter ionic distance (r_i), field strength (F), packing density (Vp), oxygen packing density (OPD), the average phosphorus-phosphorus separation ($D_{P\text{-}P}$), and the oxygen molar volume (V_O) of the glass system

Physical parameters	LiZnSiP:0Nd	LiZnSiP:0.25Nd	LiZnSiP:0.5Nd	LiZnSiP:1Nd	LiZnSiP:2Nd	LiZnSiP:4Nd
ρ (g cm^{-3}) ± 0.0013	2.545	2.551	2.557	2.570	2.595	2.644
V_m (cm^3 mol^{-1}) ± 0.0190	38.158	38.133	38.108	38.059	37.965	37.794
M_w (g mol^{-1}) ± 0.001	97.100	97.278	97.455	97.809	98.514	99.912
N_{Nd} ($\times 10^{21}$ ions cm^{-3}) ± 0.01	–	1.17	2.34	4.69	9.37	18.7
r_p (Å) ± 0.001	–	3.822	3.033	2.408	1.911	1.518
r_i (Å) ± 0.001	–	9.483	7.527	5.975	4.743	3.766
F ($\times 10^{15}$) (cm^{-2}) ± 0.01	–	3.42	5.43	8.62	13.0	21.70
$V_p \pm 0.0001$	0.5920	0.5925	0.5929	0.5938	0.5955	0.5986
OPD (g atom l^{-1}) ± 0.001	83.862	83.914	83.965	84.065	84.257	84.607
$D_{P\text{-}P}$ (Å) ± 0.001	3.987	3.985	3.983	3.979	3.972	3.959
$V_O \pm 0.001$ (cm^3 mol^{-1})	11.924	11.917	11.910	11.896	11.868	11.819

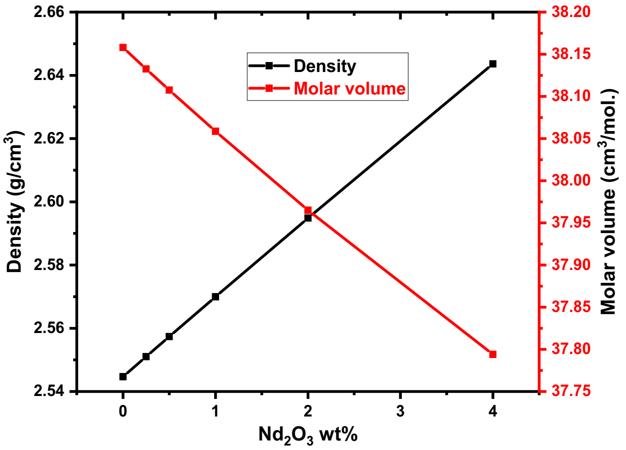

Fig. 1 Density and molar volume change with neodymium oxide content

$$r_i = \left(\frac{1}{N_{Nd}}\right)^{1/3} \tag{6}$$

$$r_p = \frac{1}{2}\left(\frac{\pi}{6N_{Nd}}\right)^{1/3} \tag{7}$$

$$F = \frac{V_{ion}}{r_P^2} \tag{8}$$

where V_{ion} is the ion's valence, N_A is the Avogadro's number.

The phosphorus–phosphorus distance ($D_{P\text{-}P}$), the packing density (V_p), and the oxygen packing density (OPD) are calculated using the formulae below [29]:

$$D_{P-P} = \left(\frac{V_m}{2N_A(1-X_P)}\right)^{1/3} \tag{9}$$

$$V_P = \frac{1}{V_m}\sum V_i X_i \tag{10}$$

$$\text{OPD} = \frac{1000 \times O}{V_m} \tag{11}$$

Also, the oxygen molar volume (V_o) is calculated using the next formula [30]:

$$V_o = \frac{V_m}{\sum X_i n_i} \tag{12}$$

where X_P is P_2O_5 mole proportion, V_i is packing factor (the data for packing factor of oxides are taken from Ref. [31]), X_i is content mole fraction, n_i is the oxygen atoms number in composition, and O is the amount of oxygen atoms in the host matrix.

All obtained values for r_p, F, N_{Nd}, and r_i are tabulated in Table 2. The observable decrease in both the r_p (from 3.822 to 1.518 Å) and r_i (from 9.483 to 3.766 Å) as Nd_2O_3 increases may be due to an increase in the value of N_{Nd} for Nd^{3+} ions. It is worth noting that the glass network will be packed with neodymium interstices, resulting in a reduction in the average Nd–O distance. As a result, the Nd–O bond strength improves, producing greater field strength (F) surrounding Nd^{3+} ions. Variations of these parameters (r_p, F, and r_i) with Nd_2O_3 content are depicted in Fig. 2.

Table 2 lists the calculated values of the OPD, V_p, and $D_{P\text{-}P}$. The values of the OPD and V_P increase from 83.862 to 84.607 g atom l^{-1} and from 0.5920 to 0.5986. Also, the values of the $D_{p\text{-}p}$ and V_o decrease from 3.987 to 3.959 Å

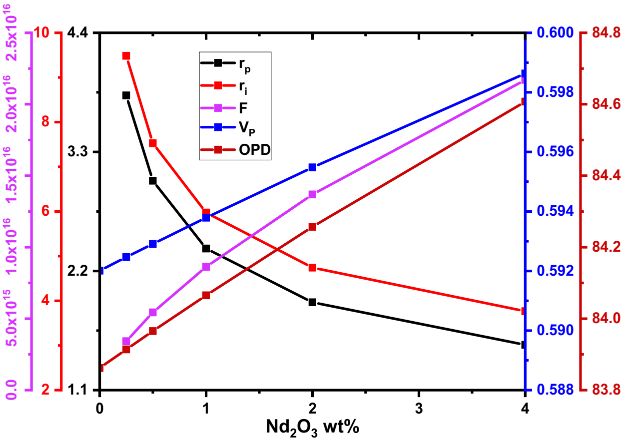

Fig. 2 Variations of r_p, r_i, F, V_p, and OPD with Nd_2O_3 content

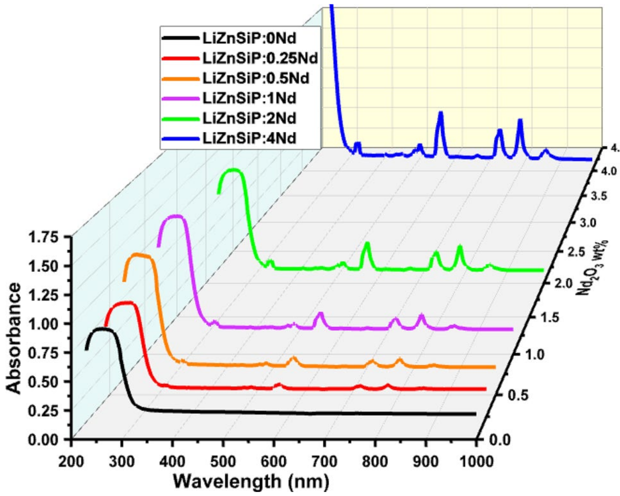

Fig. 3 UV–Vis absorption spectra for all samples

and from 11.924 to 11.819 cm^3 mol^{-1}, respectively, with the increase in Nd_2O_3 concentration (Table 2).

As seen in Fig. 2, the values of OPD increased as the content of Nd_2O_3 increased. This is due to the structural alterations in the glass matrix and the formation of additional bridging oxygen (BO). Also, the rising values of OPD with higher Nd_2O_3 concentrations indicate that the non-bridging oxygen (NBO) is not created at those concentrations and the interstitial space of the glass structure diminishes. The reduction in V_m of the glass matrix has been aided by the reduction in V_o. This has also suggested a decrease in the production of non-bridging oxygen (NBO) and excess volume in the glass matrix, which has helped to a closely packed structure in the glass network. The average $D_{P\text{-}P}$ is commonly used to investigate how the glass structure changes when the concentration of the modifiers changes. In this work, the $D_{P\text{-}P}$ values are seen to decrease as the Nd_2O_3 content increases. This confirms the V_m results and implies that the interatomic distance decreases, and thereby the compactness of the glass network increases.

3.2 The optical band gap and Urbach energy

The absorption spectra of samples doped with Nd_2O_3 (Fig. 3) reveal the main peaks at 356, 430, 476, 512, 524, 582, 683, 746, 802, and 872 nm which arise from the electronic transitions between the ground state $^4I_{9/2}$ and the excited states $^4D_{3/2}+{}^4D_{1/2}$, $^2D_{5/2}+{}^2P_{1/2}$, $^2G_{9/2}$, $^4G_{9/2}$, $^4G_{7/2}$, $^4G_{5/2}+{}^2G_{7/2}$, $^4F_{9/2}$, $^4F_{7/2}+{}^4S_{3/2}$, $^4F_{5/2}+{}^4H_{9/2}$ and $^4F_{3/2}$, respectively. The transitions are assigned by comparing the band positions in the absorption spectra with those reported in the literature [32–34].

The UV–visible spectra of the prepared samples are recorded in the wavelength range of 190–1000 nm, as seen in Fig. 3.

Davis and Mott proposed a correlation between the optical absorption coefficient (α) and incident photon energy ($h\upsilon$) [35]:

$$\alpha h\upsilon = [A(h\upsilon - E_{opt.})]^{m} \quad (13)$$

where the m is an exponent that takes the values 2 or 1/2 for an allowed indirect and direct transitions, respectively, A is constant, and $E_{opt.}$ is the optical band gap. The indirect $E_{opt.}$ are obtained by Tauc's method from Eq. (13) via the extrapolation of the linear region at $(\alpha(\upsilon)h\upsilon)^{0.5} = 0$ as shown in Fig. 4.

The values of the $E_{opt.}$ of samples are increased from 3.331 to 3.712 eV (Table 3). This rise is the result of the oxygen bond in the glass structure influencing the absorption edge (AE), and a rise in bridge density inside the glass matrix shifts the AE to lower wavelengths. In addition, replacing non-bridging oxygen (NBO) ions with bridging oxygen (BO) ions diminishes the ionic nature of the oxygen ions and the upper level of the valence band, resulting in an increase in $E_{opt.}$. Furthermore, increasing the number of bridging oxygen (BO) leads to a decrease in the number of donor centers and as a result, the $E_{opt.}$ increases. Also, the insertion of Nd^{3+} ions changes the electronic shell of O^{2-} anions, resulting in a change in the polarization of the cations, and the impurity band is broadened due to the creation of the tail at the borders of the valence and conduction bands. The similar pattern has been noticed in the previous studies [19, 36].

The disorder in amorphous substances is related to Urbach's energy (E_U) which may be determined from Fig. 5 using the formula given:

$$\ln\alpha = \ln\alpha_o + h\upsilon/E_U \quad (14)$$

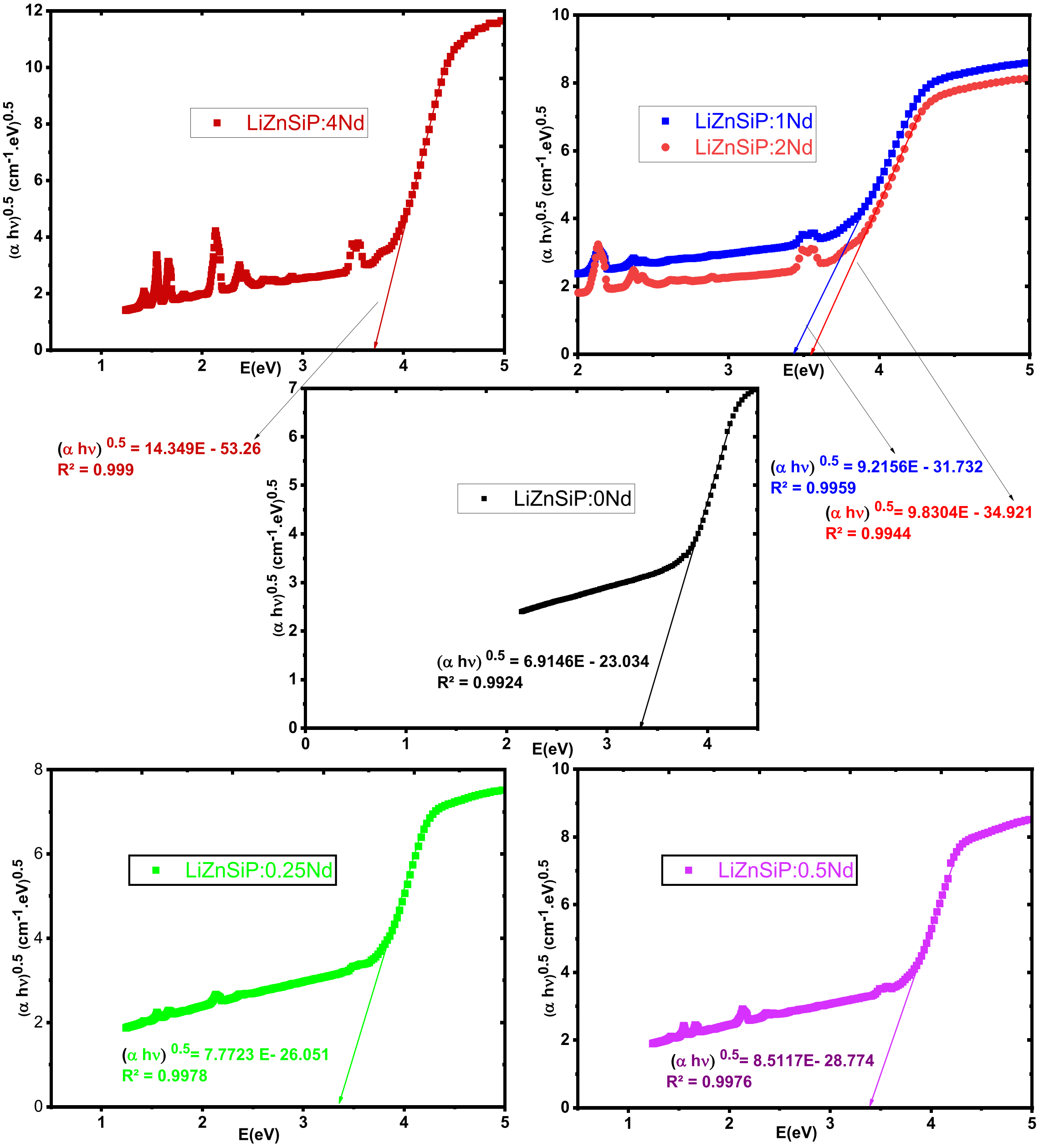

Fig. 4 Variations of $(\alpha h\nu)^{0.5}$ versus E for all samples

where α_o is constant. Table 3 displays the E_U values. The E_U is within the amorphous semiconductor's range [37].

The reduction in E_U (0.402–0.258 eV) with increasing neodymium oxide concentration may be attributed to reduced localized states and the degree of disorder in the band gap.

The steepness parameter (S) can be used to identify the broadening of the optical absorption edge caused by carrier interactions using the following relation:

$$S = \frac{K_B}{E_U}T \tag{15}$$

where T and K_B denote the room temperature and Boltzmann's constant, respectively. The S values rise from 0.064

Table 3 Optical parameters for glass samples

Parameters ± 0.001	LiZnSiP:0Nd	LiZnSiP:0.25Nd	LiZnSiP:0.5Nd	LiZnSiP:1Nd	LiZnSiP:2Nd	LiZnSiP:4Nd
$E_{\text{opt.}}$ (eV)	3.331	3.352	3.381	3.443	3.552	3.712
n	2.314	2.309	2.302	2.288	2.263	2.228
R_m (cm^3 mol^{-1})	22.588	22.526	22.442	22.275	21.970	21.516
M	0.408	0.409	0.411	0.415	0.421	0.431
ε	5.352	5.330	5.298	5.234	5.121	4.966
$\alpha_{O^{2-}}(E_{\text{opt.}})$ (Å^3)	2.781	2.773	2.762	2.740	2.701	2.641
Λ_{th}	1.205	1.207	1.209	1.213	1.222	1.238
A (Å^{-3}) × 10^{-2}	22.095	22.082	22.068	22.043	21.992	21.890
E_U (eV)	0.402	0.392	0.346	0.345	0.271	0.258
S	0.064	0.066	0.074	0.075	0.096	0.100
α_m (Å^3)	8.963	8.939	8.905	8.839	8.718	8.538
ε_{opt}	4.352	4.330	4.298	4.234	4.121	3.966
T_{opt}	0.728	0.729	0.731	0.734	0.739	0.747
R_{loss}	0.157	0.156	0.155	0.153	0.150	0.145
χ_{elect}	0.347	0.345	0.342	0.337	0.328	0.316
$\chi^{(3)}$ × 10^{-11} (esu)	0.245	0.240	0.233	0.219	0.197	0.169
$n_{\text{non-linear}}$ × 10^{-10}	0.399	0.392	0.381	0.361	0.328	0.286

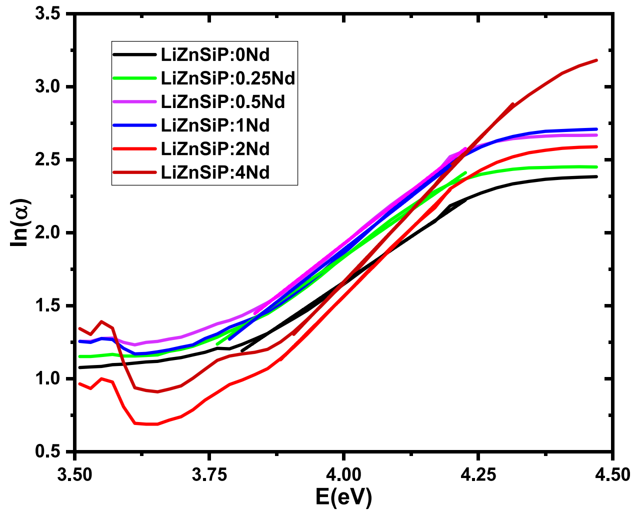

Fig. 5 Variations of ln(α) versus E for all samples

to 0.100 as the Nd_2O_3 content increases, and it has an inverse relationship to the E_U as displayed in Table 3.

3.3 Linear and non-linear optical properties

Another important property in assessing the suitability of materials for use in optical devices is the refractive index (n). It is influenced by light interactions with the electrons of the atoms that make up the glass and is dependent on the component oxides present in the glass system as well as the cationic polarizability. The n of the samples can be calculated based on the $E_{\text{opt.}}$ values and according to the following relation [38]:

$$n = \left[\frac{3 - 2\left(\frac{E_{\text{opt.}}}{20}\right)^{0.5}}{\left(\frac{E_{\text{opt.}}}{20}\right)^{0.5}} \right]^{0.5} \tag{16}$$

Table 3 presents the n values for all samples, which vary from 2.314 to 2.228. Because the rise in bridging oxygen (BO) is due to the influence of Nd_2O_3 concentration, the reducing value of n is the consequence of a modification in the ρ value, which enhances light propagation within the current glass (see Fig. 6).

Additionally, the following formulas are used to estimate the molar polarizability (α_m), molar refraction (R_m), and electronic polarizability ($\alpha_{O^{2-}}(E_{\text{opt.}})$) of an oxide ion for all glass samples [39]:

$$R_m = \frac{(n^2 - 1)}{(n^2 + 2)} V_m \tag{17}$$

$$\alpha_m = \frac{R_m}{2.52} \tag{18}$$

$$\alpha_{O^{2-}}\left(E_{\text{opt.}}\right) = \frac{\left[\left(\frac{V_m}{2.52}\right)\left(1 - \sqrt{\frac{E_{\text{opt.}}}{20}}\right) - \sum \alpha_{\text{cat.}}\right]}{N_{O^{2-}}}, \tag{19}$$

where $N_{O^{2-}}$ is the oxide ion number in the chemical formula and $\sum \alpha_{\text{cat.}}$ is the molar cation polarizability. Table 3 shows

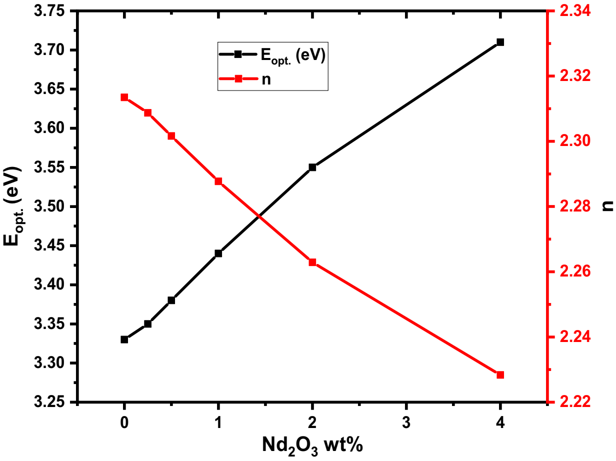

Fig. 6 Variations of $E_{opt.}$ and n with Nd_2O_3 content

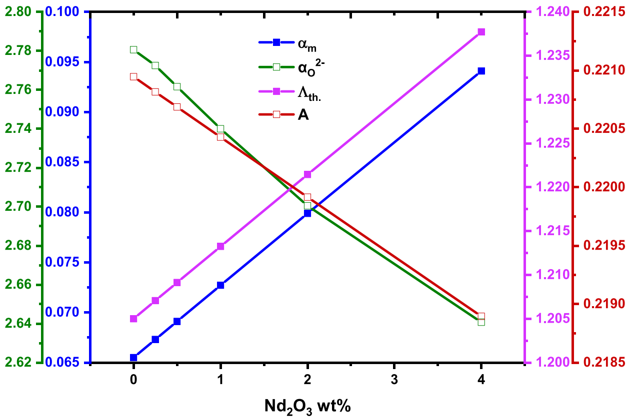

Fig. 7 Variations of α_m, $\alpha_{O^{2-}}$, $\Lambda_{th.}$, and A with Nd_2O_3 content

the values of these parameters (R_m, α_m, and $\alpha_{O^{2-}}(E_{opt.})$), which decrease from 22.588 to 21.516 (cm^3 mol^{-1}), 8.963 to 8.538 Å^3, and 2.781 to 2.641 Å^3, respectively. Changes of both α_m and $\alpha_{O^{2-}}(E_{opt.})$ with increasing content of Nd_2O_3 are shown as in Fig. 7. The decrease in these parameters with increasing Nd_2O_3 content is ascribed to an increase in the bridging oxygen (BO) in the current glass matrix.

The metallization criteria (M) defines the metallization phenomena or insulating properties of glasses and are determined as follows [40]:

$$M = \frac{V_m - R_m}{V_m} \tag{20}$$

The metallic or non-metallic nature of the materials is predicted by these conditions: $R_m/V_m \geq 1$ (metallic nature) and $R_m/V_m < 1$ (insulating nature). The M increased from 0.408 to 0.431 as the Nd_2O_3 content increased (Table 3). As a result, the present glass has an insulating nature accompanied by an increase in the $E_{opt.}$ and a decrease in the n (see Fig. 6).

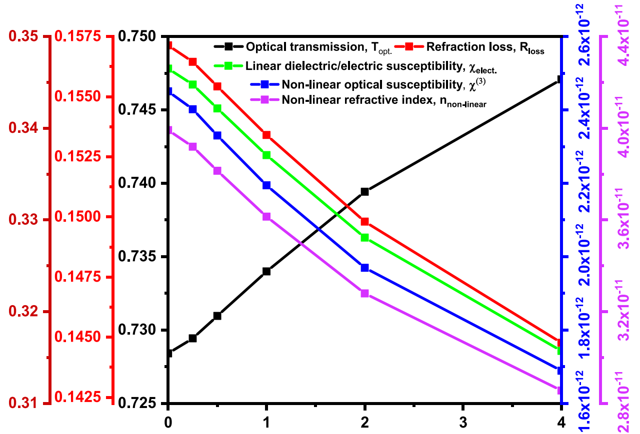

Fig. 8 Variations of $T_{opt.}$, R_{loss}, $\chi_{elect.}$, $\chi^{(3)}$, and $n_{non\text{-}linear}$ with Nd_2O_3 content

The following equations are used to estimate the reflection loss (R_{loss}), optical transmission coefficient ($T_{opt.}$), optical dielectric constant ($\varepsilon_{opt.}$), static dielectric constant (ε), electrical susceptibility (χ_{elect}), third-order non-linear susceptibility($\chi^{(3)}$), and non-linear refractive index ($n_{non\text{-}linear}$) [41, 42]:

$$R_{loss} = [(n-1)/(n+1)]^2 \tag{21}$$

$$T_{opt.} = \frac{2n}{n^2+1} \tag{22}$$

$$\varepsilon_{opt.} = \varepsilon - 1 = n^2 - 1 \tag{23}$$

$$\varepsilon = n^2 \tag{24}$$

$$\chi_{elect.} = (\varepsilon - 1)/4\pi \tag{25}$$

$$\chi^{(3)} = 1.7 \times 10^{-10} \times (\chi_{elect.})^4, \tag{26}$$

$$n_{non-linear} = \frac{12\pi\chi^{(3)}}{n}, \tag*{(26)}$$

Table 3 collects the estimated values of R_{loss}, $T_{opt.}$, $\varepsilon_{opt.}$, ε, $\chi_{elect.}$, ($\chi^{(3)}$), and $n_{non\text{-}linear}$, and these parameters (R_{loss}, $T_{opt.}$, $\varepsilon_{opt.}$, $\chi_{elect.}$, ($\chi^{(3)}$), and $n_{non\text{-}linear}$) are depicted in Fig. 8. The results indicate that R_{loss} and $T_{opt.}$ are inversely related to Nd_2O_3 content, which is consistent with the theoretical conception that $T_{opt.}$ changes inversely proportionate to R_{loss}. Furthermore, χ_{elect}, ($\chi^{(3)}$), and $n_{non\text{-}linear}$ decreased from 0.347 to 0.316, 0.245×10^{-11} to 0.169×10^{-11} esu, and 0.399×10^{-10} to 0.286×10^{-10}, respectively.

3.4 Optical basicity and interaction parameter

The optical basicity of a glass is defined by the ability of the oxide ions inside the glass to give electrons to the cations, and its theoretical value ($\Lambda_{th.}$) is estimated by [43]:

$$\Lambda_{th.} = X_{Li_2O}\Lambda_{Li_2O} + X_{ZnO}\Lambda_{ZnO} + X_{SiO_2}\Lambda_{SiO_2} + X_{P_2O_5}\Lambda_{P_2O_5} + X_{Nd_2O_3}\Lambda_{Nd_2O_3} \tag{28}$$

where $X_{Li_2O}, X_{ZnO}, X_{SiO_2}, X_{P_2O_5}$ and $X_{Nd_2O_3}$ are percentage of these oxides (Li_2O, ZnO, SiO_2, P_2O_5, and Nd_2O_3) and Λ_{Li_2O} (=0.48), Λ_{ZnO}(=0.92), Λ_{SiO_2}(= 0.48), $\Lambda_{P_2O_5}$(= 0.33), and $\Lambda_{Nd_2O_3}$ (=1.33) are the optical basicity of these oxides inside glass composition, respectively [43, 44]. The Λ_{th} values increased from 1.205 to 1.238 as listed in Table 3. The increase in the Λ_{th} values of the present glass results in a covalent enhancement of the oxygen system's cation oxygen bonds.

The interaction parameter (*A*) is used to depict the status of oxide ion polarizability, as well as the simple oxides and glasses basicity, and also the ability to create an ionic covalent bond via the cation. The *A* of the present glasses is estimated by Eq. (29):

$$\begin{aligned} A = {} & X_{Li_2O}\frac{(3.921 - \alpha_{O^{2-}})}{2(\alpha_{Li^+} + 3.921)(\alpha_{Li^+} + \alpha_{O^{2-}})} \\ & + X_{ZnO}\frac{(3.921 - \alpha_{O^{2-}})}{2(\alpha_{Zn^{2+}} + 3.921)(\alpha_{Zn^{2+}} + \alpha_{O^{2-}})} \\ & + X_{SiO_2}\frac{(3.921 - \alpha_{O^{2-}})}{2(\alpha_{Si^{2+}} + 3.921)(\alpha_{Si^{2+}} + \alpha_{O^{2-}})} \\ & + X_{P_2O_5}\frac{(3.921 - \alpha_{O^{2-}})}{2(\alpha_{P^{5+}} + 3.921)(\alpha_{P^{5+}} + \alpha_{O^{2-}})} \\ & + X_{Nd_2O_3}\frac{(3.921 - \alpha_{O^{2-}})}{2(\alpha_{Nd^{3+}} + 3.921)(\alpha_{Nd^{3+}} + \alpha_{O^{2-}})} \end{aligned} \tag{29}$$

The various polarizabilities values in Eq. (29) were obtained from Refs. [43, 44]. The estimated values of *A* were listed in Table 3. We found that increasing the Nd_2O_3 concentration decreases the *A*, which is opposite in nature to optical basicity. In Fig. 7, the correlation between *A* and $\Lambda_{th.}$ for the present glass appears, indicating the emergence of an opposing linear relationship. This behaviour is consistent with results found in previous studies [45].

3.5 Fourier transformed infrared (FTIR) spectra

The infrared spectra were recorded for all prepared samples in the energy range from 400 to 4000 cm^{-1} (as shown in Fig. 9). The following is a detailed description of all the vibration modes that appeared in these spectra:

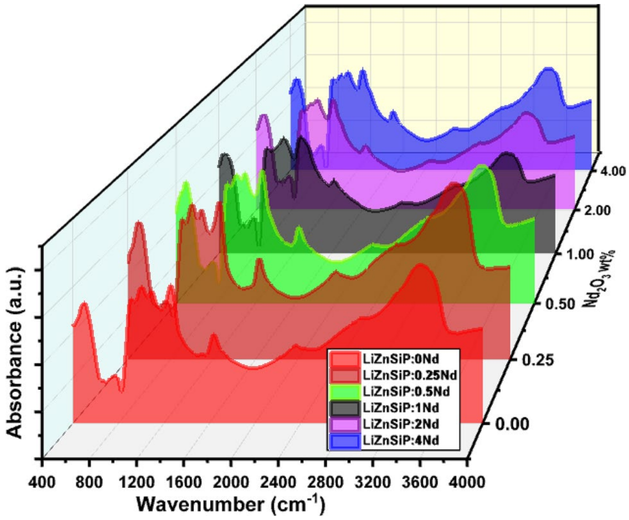

Fig. 9 FTIR absorption spectra of the LiZnSiP:Nd glasses

1. The presence of absorption bands within the spectral region 482–500 cm^{-1} arise due to the bending vibration of O–P–O unit, the ZnO tetrahedral bonds [19], the stretching vibrations (s. v.) of Nd–O bond [19], and the bending vibrations (b. v.) of Si–O–Si bonds [46].
2. The absorption bands at 659–672 cm^{-1} can be assigned to (b. v.) of Si–O–Si, to different metaphosphate groups or (b. v.) of NBO within the silicate structure and to CO_2; since carbonate (Li_2CO_3) was used to make the glass specimens, some CO_2 may have kept trapped in the glass network [47].
3. The absorption band within the region 728–741 cm^{-1} may be assigned to symmetric (s. v.) of P–O–P, υ_s (P–O–P) [19], to the Si–O–Si (b. v.) of BOs in $(SiO_4)^{4-}$ tetrahedron (Q^4) structural units creating a deformed tetrahedron [46], to symmetric stretching of (O–Si–O) bands, and to (b. v.) modes of Si–O–Si [47].
4. The absorption bands appeared at nearly 909–918 cm^{-1} is an indication of the presence of (P–O–P) as (BOs) bonds, and to the $Si–O^-$ (broken bonds) vibrations [48].
5. The absorption bands at 1000–1013 cm^{-1} can be related to asymmetric stretching of Si–O–Si in silicate network and to Si–O(Si), P–O and Si–O(P) vibrations [49].
6. The absorption bands at 1091–1095 cm^{-1} can be attributed to asymmetric (s. v.) of P–O–P groups or the sharing of antisymmetric (s. v.) of Si–O–Si [50], to the symmetric (s. v.) band of Si–O–Si, to the symmetrical (s. v.) of PO_2, $\upsilon_s(PO_2)$ [51], to asymmetric (s. v.) of $(PO_3)^{2-}$ and to $P–O^-$ symmetric stretching [52] and to symmetric (s. v.) of Si–O–Si.
7. The absorption band that exists between 1259 and 1281 cm^{-1} can be attributed to the (s. v.) of P=O [52].
8. The absorption bands detected in the region of 1630–1643 cm^{-1} are due to the (s. v.) and (b. v.) of P–O–H bridges and H_2O which is because moisture

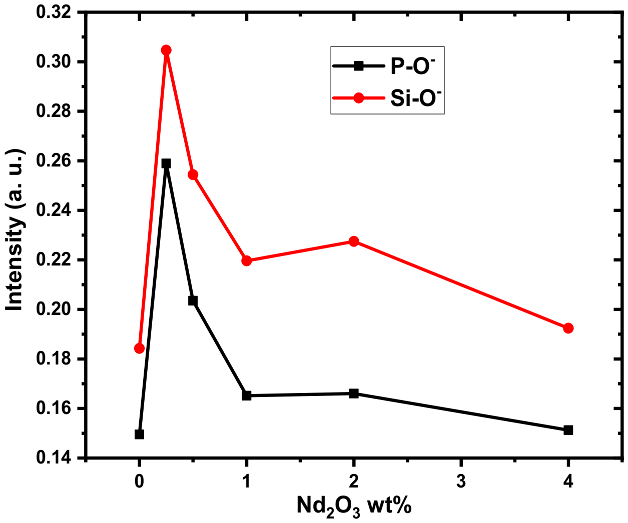

Fig. 10 The relationship between the intensities of the identified vibration modes and the Nd_2O_3 content

was absorbed during the fabrication of KBr pellets for infrared examinations and may be assigned to the hygroscopic nature of phosphate [53].

9. The absorption peaks at 2359–2376 cm^{-1} can be attributed to H_2O, OH, P–O–H, Si–OH vibrations [48, 53].
10. The existence of hydrogen bonds [53] and stretching modes of O–H bonds is responsible for the occurrence of doublet weak absorption bands seen in the regions 2846–2859 cm^{-1} and 2920–2937 cm^{-1}.
11. The broad absorption band seen in the range 3451–3489 cm^{-1} is attributed to the O–H (s. v.) of the OH group, molecular water. Also, this band may be due to P–O–H or Si–O–H vibrations [48]. The existence of OH-groups in the glass network is shown by the absorption bands at 1630–1643 and 3451–3489 cm^{-1}.

It is worth noting that, the intensity of the vibration modes for both $Si–O^-$ and $P–O^-$ increases with the first addition of Nd^{3+} ions, then this intensity decreases with the increase of these additions of Nd_2O_3 as shown in Fig. 10. This is consistent with the results mentioned above, which show an increase in the number of the BO.

3.6 Nuclear radiation shielding

To find out the protection effectiveness of prepared glass containing certain percentages of Nd_2O_3 against gamma rays and fast neutrons, the shielding nuclear parameters of the encoded samples LiZnSiP:0Nd, LiZnSiP:0.25Nd, LiZnSiP:0.5Nd, LiZnSiP:1Nd, LiZnSiP:2Nd, and LiZnSiP:4Nd, in the range of 0.015–15 MeV energy photon were obtained using Phy-X/PSD software program and compared with the results obtained from XCOM online program and the results are presented in Table 4. From Table 4, it can be noticed that the results obtained for the mass attenuation coefficient (MAC) during the two programs were somewhat identical, and there were no significant differences.

The results for the mass attenuation coefficient (MAC) of prepared glasses against the energy of gamma photon are shown in Fig. 11. The largest values of MAC were obtained at low energy 0.015 MeV and the lowest values at a photon energy of 15 MeV. As the photon energy increases higher than 0.015 MeV, the MAC of all prepared glasses decreases rapidly and this region is the photoelectric absorption interaction region (PEA) whose cross-section is proportional to $Z^{4-5}/E^{3.5}$ [54, 55]. Sudden increases in MAC values around 0.05 MeV are observed for all LiZnSiP glasses with increasing Nd_2O_3 content due to *k*-absorption edges of Nd. A clear contrast and differences in the MAC of the prepared glasses are observed in the region between 0.05 and 0.2 MeV. At energy values above 0.2 MeV, we observe a gradual decrease in the MAC values of the present glass samples and Compton scattering (CS) is dominant in this region, which is proportional to Z/E [54, 55]. Therefore, at medium and high energies, all LiZnSiP glass have approximately the same MAC values. At energies higher than 2 MeV, which is the region of the pair production (PP), the MAC values decrease very slowly. The highest values of MAC for the prepared glasses ranged between 10.99 and 13.253 $cm^2\ g^{-1}$ for LiZnSiP:0Nd–LiZnSiP:4Nd at energy 0.015 MeV, respectively. While the lowest values ranged between 0.021 and 0.022 $cm^2\ g^{-1}$ for LiZnSiP:0Nd–LiZnSiP:4Nd glasses at the energy of 15 MeV, respectively.

To compare the MAC of the present sample (LiZnSiP:4Nd) with the standard radiation shielding used in radiation protection applications such as ordinary and barite concrete (OC and BC), ferrite and chromite (Fe_2O_3 and $FeCr_2O_4$) and some types of glass (RS 360 and RS 520 G18), the results are presented in Fig. 12. From the figure, it was noticed that the values of the MAC of the prepared sample were higher than those of ordinary concrete (OC) and Rs 520 G18 glass at low energy values. While the MAC values for the present sample were less than the values of the barite concrete (BC), ferrite and chromite, and RS 360 glass.

The half-value layer (HVL) is the thickness of the material that reduces the intensity of the incident beam of gamma rays by half. Figure 13 shows the variation in the HVL of the prepared samples with photon energy. According to Fig. 13, the lowest values of the HVL were at the low energy of the photon and then gradually increased as the energy of the photon increased until it reached the value of 0.8 MeV. After that, the values increase rapidly until they reach the highest value at the energy of 15 MeV. The lowest values for the HVL were for sample LiZnSiP:4Nd, which means that it has

Table 4 MAC of the LiZnSiP:0Nd–LiZnSiP:4Nd glasses obtained by XCOM and Phy-X programs with different photons energies

Energy	LiZnSiP:0Nd		LiZnSiP:0.25Nd		LiZnSiP:0.5Nd		LiZnSiP:1Nd		LiZnSiP:2Nd		LiZnSiP:4Nd	
	XCOM	Phy-X	XCOM	Phy-X	XCOM	Phy-X	XCOM	Phy-X	XCOM	Phy-X	XCOM	Phy-X
0.015	10.990	10.990	11.190	11.140	11.260	11.283	11.570	11.573	12.130	12.144	13.300	13.253
0.02	4.934	4.932	5.025	5.002	5.058	5.069	5.203	5.205	5.467	5.473	6.015	5.991
0.03	1.642	1.642	1.673	1.666	1.685	1.688	1.734	1.735	1.824	1.825	2.009	2.002
0.04	0.802	0.802	0.817	0.813	0.822	0.824	0.845	0.845	0.886	0.887	0.972	0.969
0.05	0.494	0.494	0.536	0.529	0.562	0.564	0.631	0.633	0.768	0.770	1.041	1.035
0.06	0.353	0.353	0.379	0.375	0.396	0.397	0.439	0.440	0.524	0.525	0.695	0.691
0.08	0.236	0.236	0.248	0.246	0.255	0.256	0.275	0.276	0.315	0.315	0.393	0.392
0.1	0.189	0.189	0.196	0.195	0.200	0.200	0.211	0.211	0.232	0.232	0.275	0.274
0.15	0.145	0.145	0.147	0.147	0.148	0.148	0.152	0.152	0.159	0.159	0.173	0.172
0.2	0.126	0.126	0.127	0.127	0.128	0.128	0.130	0.130	0.133	0.133	0.139	0.139
0.3	0.107	0.107	0.107	0.107	0.107	0.107	0.108	0.108	0.109	0.109	0.110	0.110
0.4	0.095	0.095	0.095	0.095	0.095	0.095	0.095	0.095	0.095	0.095	0.096	0.096
0.5	0.086	0.086	0.086	0.086	0.086	0.086	0.086	0.086	0.086	0.086	0.087	0.087
0.6	0.079	0.079	0.079	0.079	0.080	0.079	0.080	0.080	0.080	0.080	0.080	0.080
0.8	0.070	0.070	0.070	0.070	0.070	0.070	0.070	0.070	0.070	0.070	0.070	0.070
1	0.063	0.063	0.063	0.063	0.063	0.063	0.063	0.063	0.063	0.063	0.063	0.063
1.5	0.051	0.051	0.051	0.051	0.051	0.051	0.051	0.051	0.051	0.051	0.051	0.051
2	0.044	0.044	0.044	0.044	0.044	0.044	0.044	0.044	0.044	0.044	0.044	0.044
3	0.036	0.036	0.036	0.036	0.036	0.036	0.036	0.036	0.036	0.036	0.036	0.036
4	0.031	0.031	0.031	0.031	0.031	0.031	0.031	0.031	0.031	0.031	0.032	0.032
5	0.028	0.028	0.029	0.028	0.029	0.029	0.029	0.029	0.029	0.029	0.029	0.029
6	0.027	0.027	0.027	0.027	0.027	0.027	0.027	0.027	0.027	0.027	0.027	0.027
8	0.024	0.024	0.024	0.024	0.024	0.024	0.024	0.024	0.024	0.024	0.025	0.025
10	0.023	0.023	0.023	0.023	0.023	0.023	0.023	0.023	0.023	0.023	0.024	0.024
15	0.021	0.021	0.021	0.021	0.021	0.021	0.022	0.022	0.022	0.022	0.022	0.022

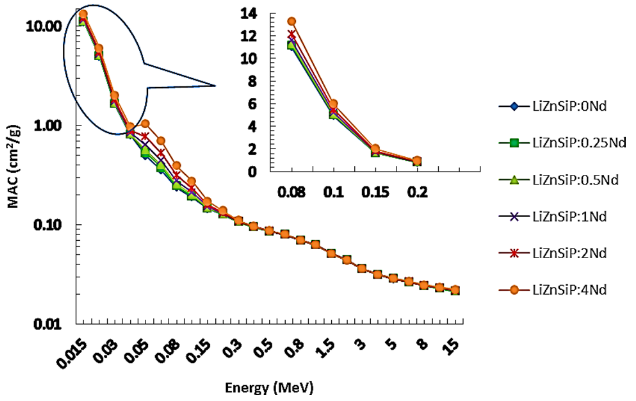

Fig. 11 MAC for prepared glass samples

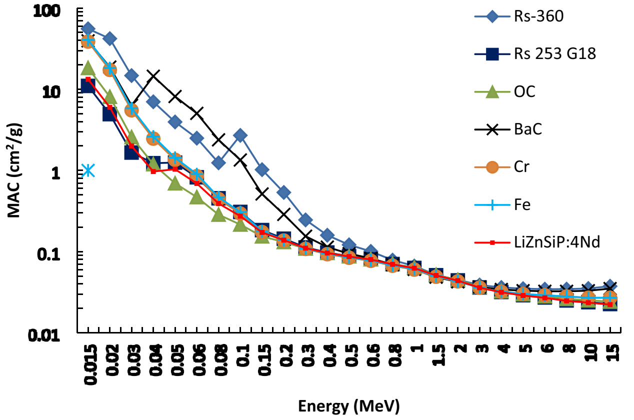

Fig. 12 Comparison of the minimum and maximum values of the MAC of the prepared samples and commercial materials

the best protection from gamma rays among the studied samples, and the highest values were for sample LiZnSiP:0Nd. The values of the HVL were about 0.025, 0.024, 0.024, 0.023, 0.022, and 0.019 cm at energy 15 keV, while they were 12.76, 12.69, 12.63, 12.50, 12.25, and 11.78 cm at energy 15 MeV for samples LiZnSiP:0Nd, LiZnSiP:0.25Nd, LiZnSiP:0.5 N, LiZnSiP:1Nd, LiZnSiP:2Nd, and LiZnSiP:4Nd, respectively.

Mean free path (MFP) defines the distance traveled between two successive collisions of gamma photons. Figure 14 presents the MFP values of the present glasses with

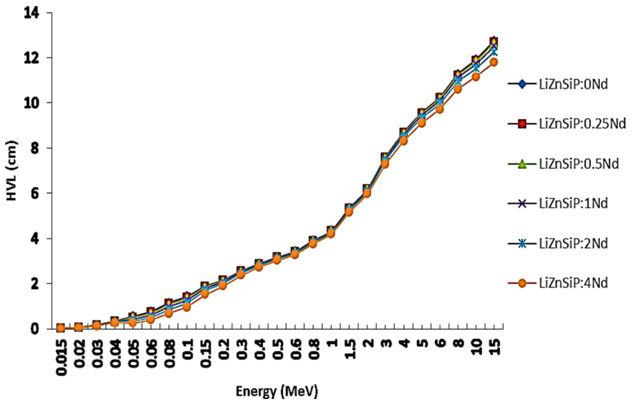

Fig. 13 HVL for prepared glass samples

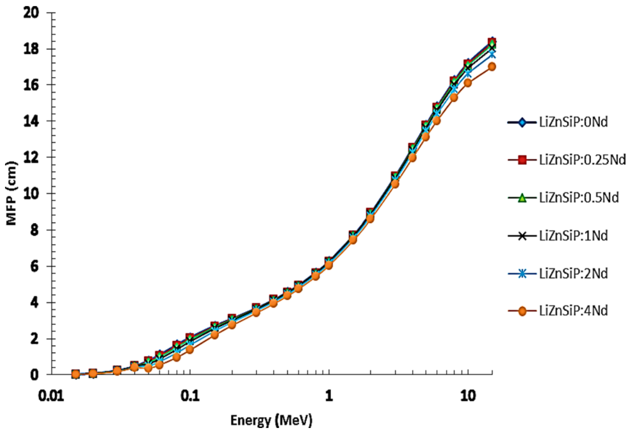

Fig. 14 MFP for prepared glass samples

photon energy. Small MFP values mean that the shielding material is better at attenuating gamma photons. In Fig. 14, it can be seen that the lowest values were at the low energies of the photon, while the highest values were at the high energy values of the photon. It can be noticed that the behavior of the MFP with energy is similar to the behavior of the HVL with photon energy. The MAC values were about 0.036, 0.035, 0.034, 0.033, 0.031, and 0.028 cm at 15 keV, while they were 18.41, 18.31, 18.22, 18.03, 17.67, and 16.66 cm at energy of 15 MeV for LiZnSiP:0Nd, LiZnSiP:0.25Nd, LiZnSiP:0.5 N, LiZnSiP:1Nd, LiZnSiP:2Nd, and LiZnSiP:4Nd present glasses, respectively.

The effective atomic number (Z_{eff}) is used to represent materials containing several elements with one atomic number, especially in biology and medical applications, and it varies with the photon energy. The effective atomic number (Z_{eff}) was calculated using the Phy-X/PSD program. Figure 15 presents the varying Z_{eff} values for prepared glasses with photon energy. As shown in Fig. 15, the highest values

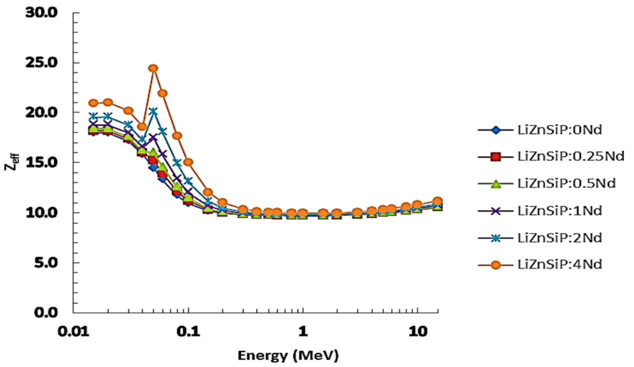

Fig. 15 Z_{eff} for prepared glass samples

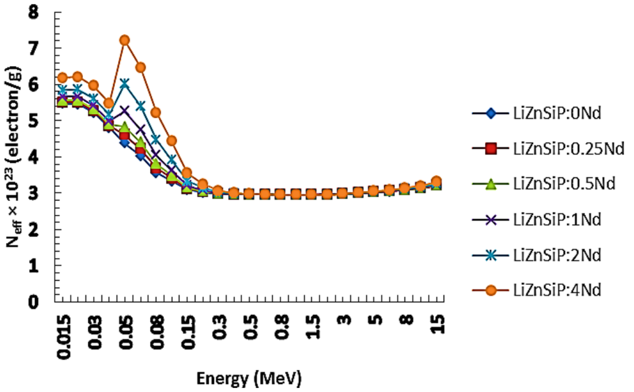

Fig. 16 N_{eff} for prepared glass samples

for Z_{eff} were in the lower energy region due to the PEA process and a sudden drop in Z_{eff} values towards 0.2 MeV of photon energy is observed. The appearance of a sudden increase and a sharp peak at the energy value of 50 keV is the *k*-absorption edge of the Nd element. It is also noticed that the Z_{eff} values increase with increasing the content of Nd_2O_3 in the prepared glass. At medium energies, the Z_{eff} values for all present glasses are constant and then increase slightly at higher energies. The values of Z_{eff} for the prepared glass samples ranged between 17.97 and 20.92 at energy 15 keV, while it reached 10.54–11.20 at energy 15 MeV, for LiZnSiP:0Nd–LiZnSiP:4Nd present glasses, respectively.

In addition to the effective atomic number, the electron density (N_{eff}) of the prepared glass samples was also obtained. Figure 16 shows the electron density varying of prepared glass samples with photon energy. From Fig. 16, it is clear that the behavior of electron density with energy is similar to that of the effective atomic number. It was found that the N_{eff} value of the prepared glass has a maximum value at energy 0.015 MeV and is equal to (5.46, 5.51, 5.56, 5.65, 5.84, and 6.18) $\times 10^{23}$ electron g^{-1}, while the values were equal to (3.20, 3.21, 3.22, 3.23, 3.25,

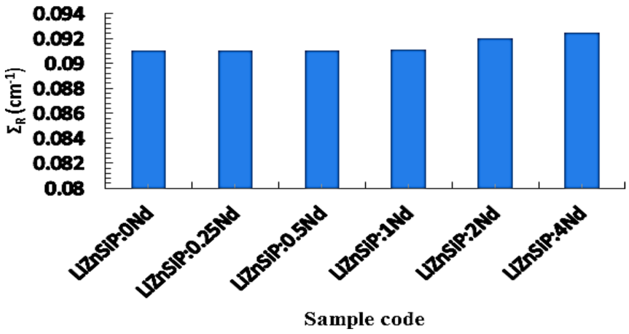

Fig. 17 The effective removal cross-section for fast neutron (Σ_R) for all prepared samples

and 3.31) × 10^{23} electron g^{-1} at energy 15 MeV, for the LiZnSiP:0Nd–LiZnSiP:4Nd prepared glasses, respectively.

Besides finding the nuclear radiation shielding parameters, the protective ability of the prepared glasses against uncharged particles (fast neutrons) was also evaluated. For this purpose, the macroscopic removal cross-section (Σ_R) of the glasses for fast neutrons was calculated. Effective removal of neutron cross-section refers to the process of removing neutrons from materials at the appropriate time. The Σ_R values are a measure of the interaction probability between the fast neutrons and the target. The Σ_R values for a substance can be calculated using the following equation [27]:

$$\sum_R = \sum w_i \left(\sum_{R/\rho} \right) \tag{30}$$

where w_i is partial density (g cm^{-3}) of the ith element and $\Sigma_{R/\rho}$ is mass removal cross-section (cm^2 g^{-1}).

The values of Σ_R for the prepared glasses are presented in Fig. 17. The Σ_R values increased with increasing density with the addition of Nd_2O_3. The Σ_R values were found to be 0.0910, 0.0910, 0.0910, 0.0911, 0.0920, and 0.0925 cm^{-1} for the LiZnSiP:0Nd–LiZnSiP:4Nd prepared glasses, respectively. The best values were for sample LiZnSiP:4Nd, which is close to the recorded value of 0.101 for water and paraffin.

4 Conclusions

The conclusions of the current study are summarized in the following points: The present glass system was successfully prepared, and the well-known Archimedes method was used to measure the density, which increased from 2.545 to 2.644 g cm^{-3}, while the molar volume decreased from 38.158 to 37.794 cm^3 mol^{-1}. The increase in the density was attributed to an increase in the molecular weight of Nd_2O_3 compared to the molecular weights of the rest of the glass-forming oxides. Many physical properties such as polaron radius, field strength, and oxygen-packing density were calculated, and the results explained the effect of adding Nd_2O_3 inside the prepared glass. Depending on the recording of optical spectra in the ultraviolet and visible regions, the values of the optical gap energies of the samples were determined, and it was found that they increased from 3.331 to 3.712 eV with the addition of Nd^{3+} ions. The results of the infrared spectra analysis showed many vibration modes, and it was found that the intensity of both P–O^- and Si–O^- vibration modes decreases with the increase of Nd^{3+} ions, which confirms the increase in the bridging oxygen (BO). With increasing Nd_2O_3 content, the theoretical optical basicity ($\Lambda_{th.}$) values increased from 1.205 to 1.238, while the interaction (A) values decreased from 0.2209 to 0.2189 Å^3.The maximum values of the MAC and the MFP of the gamma reaction occurred at the low energy of 15 keV, while the lowest value for the HVL was at the same energy. On the other hand, the lowest values of the above-mentioned parameters occurred at an energy of 15 MeV. The maximum Z_{eff} and N_{eff} values for the gamma reaction occurred at 0.05 MeV and the Z_{eff} values increased from 14.4 to 20.1 with Nd_2O_3 increasing from 0 to 4 wt%. The Nd_2O_3 content affected the gamma-protective properties of the prepared glasses. In contrast, the effective removal cross-section for fast neutrons increased from 0.0910 to 0.0925 cm^{-1} with increasing Nd_2O_3 content.

Data availability Analysed data supporting the findings of this study are available from the corresponding author on request.

References

1. G. Moulika, S. Sailaja, B.N.K. Reddy, V.S. Reddy, S. Dhoble, B.S. Reddy, Phys. B **535**, 2–7 (2018)
2. M.K. Hwang, I.G. Kim, B.K. Ryu, Study of water resistance of Fe_2O_3 doped $P_2O_5eZnOeBi_2O_3$ sealing glass system Korean. J. Met. Mater. **54**, 621–625 (2016)
3. M. Saad, H. Elhouichet, J. Alloy. Compd. **806**, 1403–1409 (2019)
4. S. Reis, M. Karabulut, D. Day, J. Non Cryst. Solids **292**, 150–157 (2001)
5. L. Yu, S.X. Zhao, X. Wu, J.W. Li, E.L. Zhao, G.D. Wei, J. Alloy. Compd. **810**, 151938 (2019)
6. X. Wu, S.X. Zhao, L.Q. Yu, J.W. Li, E.L. Zhao, C.W. Nan, Electrochim. Acta **297**, 872–878 (2019)
7. M. He, J. Jia, J. Zhao, X. Qiao, Du. Jincheng, X. Fan, Ceram. Int. **47**, 2963–2980 (2021)
8. S.K. Mahamuda, F. Syed, C.B. Annapurnadevi, K. Swapna, M.V.V.K.S. Prasad, M. Venkateswarlu, A.S. Rao, J. Non Cryst. Solids **555**, 120538 (2021)
9. K.A. Mahmoud, F.I. El-Agwany, Y.S. Rammah, O.L. Tashlykov, J. Non Cryst. Solids **541**, 120110 (2020)

10. H. Takebe, Y. Baba, M. Kuwabara, J. Non-Cryst, Solids **352**, 3088–3094 (2006)
11. E. Mansour, G. El-Damrawi, Phys. B **405**, 2137–2143 (2010)
12. P. Pascuta, G. Borodi, N. Jumate, I. Vida-Simiti, D. Viorel, E. Culea, J. Alloy. Compd. **504**, 479–483 (2010)
13. G. Walter, U. Hoppe, J. Vogel, G. Carl, P. Hartmann, J. Non-Cryst, Solids **333**, 252–262 (2004)
14. K. Kirdsiri, J. Kaewkhao, N. Chanthima, P. Limsuwan, Ann. Nucl. Energy **38**, 1438–1441 (2011)
15. C. Liu, R. Zhang, X. Zhao, J. Jia, Y. Min, J. Non Cryst. Solids **557**, 120579 (2021)
16. E.E. Saleh, M.A. Algradee, S.A. El-Fiki, G.M. Youssef, Radiat. Phys. Chem. **193**, 109939 (2022)
17. E.E. Saleh, M.A. Algradee, M.S. Al-Fakeh, Radiat. Phys. Chem. **189**, 109743 (2021)
18. M.A. Algradee, E.E. Saleh, O.M. Samir, A.B. Alwany, T.M. El Sherbini, J. Non Cryst. Solids **576**, 121304 (2022)
19. M.A. Algradee, E.E. Saleh, T.M. El Sherbini, R. El-Mallawany, Optik **242**, 167059 (2021)
20. M.A. Algradee, A. Elwhab, B. Alwany, M. Sultan, M. Elgoshimy, Q. Almoraisy, Optik **142**, 13–22 (2017)
21. M. Algradee, M. Sultan, O.M. Samir, A. Elwhab, B. Alwany, Appl. Phys. A **123**(524), 1–12 (2017)
22. V.B. Sreedhar, R. Doddoji, K. Kiran Kumar, V.R.M. Reddy, J. Non Cryst. Solids **553**, 120521 (2021)
23. M.A. Algradee, A.B. Alwany, O.M. Samir, E.E. Saleh, T.M. El Sherbini, Non Cryst. Solids **589**, 121664 (2022)
24. E. Sakar, Ö.F. Özpolat, B. Alım, M.I. Sayyed, M. Kurudirek, Radiat. Phys. Chem. **166**, 108496 (2020)
25. M.J. Berger, J.H. Hubbell, XCOM: photon cross sections database. National Institute of Standards and Technology, Gaithersburg, 1987–1999. Web version 1.2.
26. G.P. Singh, J. Singh, P. Kaur, S. Kaur, D. Arora, R. Kaur, K. Kaur, D.P. Singh, J. Mater. Res. Technol. **9**(6), 14425–14442 (2020)
27. E.E. Saleh, M.A. Algradee, F. Alresheedi, M.S. Al-Fakeh, S.A. El-Fiki, G.M. Youssef, T.M. El Sharbini. J. Electron. Mater. (2022).
28. K. Annapurna, S. Buddhudu, J. Solid State Chem. **93**, 454–460 (1991)
29. V.C. Veeranna Gowda, Phys. B **426**, 58–64 (2013)
30. M.Ç. Ersundu, A.E. Ersundu, M.I. Sayyed, J. Alloy. Compound. **714**, 278–286 (2017)
31. S. Inaba, S. Fujino, K. Morinaga, J. Am. Ceram. Soc. **82**, 3501–3507 (1999)
32. Fu. Yuanlin Wang, Q.W. Wang, H. Zhu, G. Xiang, Q. Liao, Y. Zhu, J. Non Cryst. Solids **526**, 119726 (2019)
33. F.H. ElBatal, S. Ibrahim, A.M. Abdelghany, J. Mol. Struct. **1030**, 107–112 (2012)
34. N. Chanthima, N. Sangwaranatee, Adv. Mater. Res. **979**, 390–394 (2014)
35. N.F. Mott, E.A. Davis, *Electronic Process in the Non Crystalline Materials*, 2nd edn. (Clarendon Press/Oxford University, New York, 1979)
36. S.B. Kolavekar, N.H. Ayachit, Mater. Chem. Phys. **257**, 123796 (2021)
37. E. Davis, N.F. Mott, Philos. Mag. **22**, 903–922 (1970)
38. V. Dimitrov, S. Sakka II., J. Appl. Phys. **79**, 1741–1745 (1996)
39. E.A. Moelwyn-Hughes, *Physical Chemistry* (Pergamon, London, 1961)
40. S.S. Rao, G. Ramadevudu, M. Shareefuddin, A. Hameed, M.N. Chary, M.L. Rao, Int. J. Eng. Sci. Technol. **4**, 25–35 (2012)
41. R. Mondal, D. Biswas, A.S. Das, R.K. Nanaoningthemcha, D. Deb, S. Bhattacharya, S. Kabi, Mater. Chem. Phys. **255**, 123561 (2020)
42. A.A. Ali, Y.S. Rammah, M.H. Shaaban, J. Non-Cryst, Solids **514**, 52–59 (2019)
43. V. Dimitrov, T. Komatsu, J. Univ. Chem. Technol. Metall. **45**, 219–250 (2010)
44. X. Zhao, X. Wang, H. Lin, Z. Wang, Phys. B **392**, 132–136 (2007)
45. B.E. Roopa, J. Non Cryst. Solids **551**, 120394 (2021)
46. M. Bala, S. Pawaria, N. Deopa, S. Dahiya, A. Ohlan, R. Punia, A.S. Maan, J. Mol. Struct. **1234**, 130160 (2021)
47. Y.M. Hamdy, M.A. Marzouk, H.A. El Batal, Phys. B **429**, 57–62 (2013)
48. A.M. Abdelghany, F.H. El Batal, H.A. El Batal, F.M. Ezz El Din, J. Mol. Struct. **1074**, 503–510 (2014)
49. J. Sułowska, I. Wacławska, Z. Olejniczak, Vib. Spectrosc. **65**, 44–49 (2013)
50. A.M. Abdelghany, H.A. ElBatal, J. Mol. Struct. **1024**, 47–53 (2012)
51. L. Koudelka, L. Mošner, Mater. Lett. **42**, 194–199 (2000)
52. Y.S. Rammah, F.I. El-Agawany, K.A. Mahmoud, R. El-Mallawany, E. Ilik, G. Kilic, J. Mater. Sci. Mater. Electron. **31**, 9099–9113 (2020)
53. M.A. Algradee, Y.H. Elbashar, S. Wageh, H.H. Hassan, J. Opt. **50**, 381–394 (2021)
54. G.P. Singh, J. Singh, P. Kaur, T. Singh, R.K.S. Kaur, D.P. Singh, J. Alloy. Compd. **885**, 160939 (2021)
55. M.S. Al Buriahi, Y.S.M. Alajerami, A.S. Abouhaswa, A. Alalawi, T. Nutaro, B. Tonguc, J. Non Cryst. Solids **544**, 120171 (2020)